Geometric origin of oxygen ordering and the solubility limit in niobium

Dingxin Fan [1,*] Guangming Cheng [1,*] Kyle Zhao [2] and Nan Yao [1,†]
[1]*Princeton Materials Institute, Princeton University, Princeton, New Jersey 08540, USA*
[2]*School of Computing, Information and Data Sciences, University of California San Diego, La Jolla, California 92093, USA*

(Received 7 May 2026; accepted 29 September 2026; published 4 November 2026)

We investigate early-stage Nb oxidation by combining first-principles calculations with high-resolution transmission electron microscopy. An ordered ε phase is identified, in which O atoms occupy octahedral interstitial sites in an alternating layered configuration. Oxygen incorporation proceeds through geometrically open surface sites and is directed toward octahedral interstitial sites. A descriptor-based analysis shows that O–O separations within this interstitial sublattice capture the dominant trend in incorporation stability. As oxygen concentration increases, unfavorable short-range O–O interactions become unavoidable, leading to a rapid increase in free energy and providing a geometric mechanism that limits further oxygen incorporation.

DOI: 10.1103/3l34-v1x8

I. INTRODUCTION

The interaction of oxygen with body-centered cubic (bcc) metals is a problem of broad scientific and technological significance, governing high-temperature oxidation, corrosion resistance, and hydrogen embrittlement in structural alloys [1,2]. A characteristic feature of bcc metal-oxygen systems is the remarkable diversity of oxide phases that can form, including oxygen-deficient suboxides, stoichiometric compounds, and phases with complex crystallographic structures [3–9]. Interstitial ordering of oxygen in bcc metals has been recognized for decades: Superlattice reflections attributed to ordered oxygen arrangements have been observed in niobium (Nb), vanadium (V), tantalum (Ta), etc. [10–13]. However, the precise atomic structure of many of these ordered phases—and the physical principles that govern their stability—has yet to be established.

Nb is a technologically important bcc metal, widely utilized in superconducting radio-frequency cavities, high-temperature structural applications, and corrosion-resistant systems owing to its combination of mechanical strength, thermal stability, and electronic properties [14–19]. The Nb–O system is particularly complex: Nb oxides form a rich family of phases and polymorphs, and previous studies have reported contradictory results [20]. Under oxygen-rich conditions, Nb forms a series of stable oxides, including NbO, NbO_2, and Nb_2O_5, which have been extensively studied in both bulk and thin-film forms [21–23]. In addition, Nb–O systems are known to exhibit a variety of oxygen-deficient suboxide phases with complex crystallographic structures [3]. At low oxygen concentrations, oxygen atoms occupy interstitial positions within the Nb lattice. The reported O solubility depends strongly on temperature and preparation method, with O concentrations up to $NbO_{0.17}$ (14.5 at. % O) reported for electrolytically prepared Nb(O) solid solutions [24], while equilibrium solubilities are generally lower [25]. Similar oxidation complexity is also observed in other bcc metals [7,26]. Although interstitial ordering in Nb–O has been observed and surface adsorption and diffusion have been studied extensively [27–32], the precise atomic structure of the ordered phases that emerge during early oxidation, and the physical mechanism governing their stability and the observed concentration limit, have remained unresolved.

In this work, we combine high-resolution transmission electron microscopy (HRTEM) with corresponding image simulations, together with density functional theory (DFT) calculations, to investigate oxygen incorporation in Nb. We identify a previously unreported ordered ε phase that emerges during the early-stage oxidation of Nb and determine its atomic structure through combined experimental and theoretical analysis. DFT calculations are then employed to understand the physical origin and stability of this structure.

To understand why this ordering emerges, we analyze oxygen incorporation pathways, interstitial-site energetics, and concentration-dependent thermodynamic stability. Our analysis shows that the alternating layered configuration accommodates local structural distortions without requiring significant global lattice deformation, thereby enabling the formation of a metastable phase. Oxygen in Nb preferentially occupies octahedral interstitial sites (OIS), as reported in previous theoretical [32] and experimental [33,34] studies. Our calculations confirm this preference and further show, through structural relaxation, that it is associated with the local Nb–O bonding environments in the ε phase. As more oxygen is incorporated, not all atoms can maintain these favorable environments simultaneously, and configurations with short O–O separations become unavoidable. This leads to a rapid increase in free energy with oxygen concentration, providing a microscopic, geometry-based mechanism for the experimentally observed solubility limit.

These results provide a consistent physical picture of oxygen incorporation, ordering, and stability in Nb. Oxy-

*These authors contributed equally to this work.
†Contact author: nyao@princeton.edu

Published by the American Physical Society under the terms of the Creative Commons Attribution 4.0 International license. Further distribution of this work must maintain attribution to the author(s) and the published article's title, journal citation, and DOI.

gen incorporation is selectively guided by wider surface openings, which provide pathways into subsurface regions connected to favorable OIS configurations. Once incorporated, oxygen is stabilized in an alternating layered ε phase, where O-free Nb layers buffer local O-induced distortions between O-containing layers. At higher oxygen concentrations, short O–O separations become increasingly unavoidable, leading to a rapid increase in oxygen incorporation free energy. This geometry-driven framework links surface entry, interstitial-site preference, oxygen ordering, and concentration-dependent stability in Nb, and may provide a useful perspective for other bcc metal-oxygen systems.

II. METHODS

A. Computational details

We employ a real-space pseudopotential DFT code, PARSEC [35,36], for all electronic structure calculations. The convergence criterion of the self-consistent residual error is 2×10^{-4} Ry (0.002 72 eV). The grid spacing is 0.16 Å. We incorporate Troullier-Martins norm-conserving pseudopotentials [37]. We use the local density approximation by Perdew-Wang [38] for the exchange-correlation functional, following our previous Nb surface calculations [30]. Monkhorst-Pack k-point grids [39] ($8 \times 12 \times 1$) and ($4 \times 4 \times 4$) are used for Brillouin zone integration for slab and bulk calculations, respectively.

We model the Nb(110) surface as a four-layer 2×2 slab with a bcc structure, using a supercell with $a = 6.55$ Å, $b = 4.63$ Å, and a slab width of 22.54 Å, with a vacuum layer of 15.60 Å. We keep the optimized O_2 bond length (1.19 Å) constant. After bond dissociation, we study the adsorption of atomic O.

The adsorption energy, E_{ad}, is calculated using

$$E_{\mathrm{ad}} = E_{\mathrm{sys}} - \left(E_{\mathrm{Nb(110)}} + E_{\mathrm{O_2/O}}(\vec{R})\right), \tag{1}$$

where E_{sys}, $E_{\mathrm{Nb(110)}}$, and $E_{\mathrm{O_2/O}}(\vec{R})$ represent the calculated electronic energies of the system, the bare surface, and the isolated O_2 or atomic O located at the corresponding adsorption position, $\vec{R}$, respectively. Accounting for the $\vec{R}$ dependence of the total energy of the O_2 molecule eliminates any artifacts associated with the energy changing for an isolated molecule when it is moved over the real-space grid [30,40].

The net magnetic moment (NMM) of the system is calculated through the integration of the difference in spin-up, $\rho_{\uparrow}(\vec{r})$, and spin-down, $\rho_{\downarrow}(\vec{r})$, electron densities over the full domain, Ω, using [41]

$$\mathrm{NMM} = \left| \int_{\Omega} [\rho_{\uparrow}(\vec{r}) - \rho_{\downarrow}(\vec{r})] \mathrm{d}^3 r \right|. \tag{2}$$

Bulk Nb is modeled using a $2 \times 2 \times 2$ bcc supercell with supercell lattice vectors of 6.55 Å. O atoms are placed at either OIS or tetrahedral interstitial sites (TIS) to represent Nb–O configurations at different concentrations. The effect of supercell size is further examined using $1 \times 1 \times 1$ and $4 \times 4 \times 4$ cells, as discussed in Appendix C. We perform structural relaxations with a maximum residual force of 0.01 Ry/a.u., which allows us to retain distinct local configurations for comparison.

The formation energy per O atom is calculated as

$$E(\mathrm{formation}) = \frac{E_{\mathrm{Nb}_x\mathrm{O}_n} - E_{\mathrm{Nb}_x} - \frac{n}{2}E_{\mathrm{O_2}}}{n}, \tag{3}$$

where $E_{\mathrm{Nb}_x\mathrm{O}_n}$ is the energy of the oxygen-containing supercell, E_{Nb_x} is the energy of the supercell, $E_{\mathrm{O_2}}$ is the energy of an isolated O_2, and x and n are the number of Nb and O atoms in the supercell, respectively.

A two-dimensional potential energy surface (PES) scan is performed to characterize the penetration pathway. The force acting on O is obtained from the negative gradient of the PES.

The change in Gibbs free energy is calculated per O atom as

$$\Delta G(n,\ T,\ p) = \frac{E_{\mathrm{Nb}_x\mathrm{O}_n} - E_{\mathrm{Nb}_x} - n\mu_{\mathrm{O}}(T,p)}{n}, \tag{4}$$

where the oxygen chemical potential is defined as

$$\mu_{\mathrm{O}}(T,p) = \tfrac{1}{2}[E_{\mathrm{O_2}} + \Delta\mu_{\mathrm{O_2}}(T,p)], \tag{5}$$

with

$$\Delta\mu_{\mathrm{O_2}}(T,p) = [H(T) - H(0)] - TS(T) + k_B T \ln\left(\frac{p}{p_0}\right). \tag{6}$$

Here, $H(T)$ and $H(0)$ are the enthalpies of gaseous O_2 at temperature T and 0 K, respectively, and $S(T)$ is the entropy of gaseous O_2 at temperature T. Thermodynamic corrections are taken from the NIST-JANAF tables at $T = 298.15$ K and $p_0 = 1$ bar. We neglect vibrational contributions from the solid phase.

To quantify the effect of oxygen distribution on thermodynamic stability, we characterize each oxygen configuration using three geometric parameters: N_a, $N_{\sqrt{2}a}$, and $N_{\sqrt{3}a}$, corresponding to the numbers of O–O pairs separated by different distances, where a (≈3.3 Å) is the nearest-neighbor O–O separation on the octahedral interstitial sublattice defined by the underlying Nb lattice. The fitted Gibbs free energy per O is expressed using a linear model,

$$\Delta G = \alpha + c_1 N_a + c_2 N_{\sqrt{2}a} + c_3 N_{\sqrt{3}a}. \tag{7}$$

The coefficients are obtained by least-squares fitting to DFT-calculated ΔG values using the pair counts listed in Table I. These coefficients have units of eV per pair and describe how each class of O–O separation correlates with the stability of oxygen configurations within the selected OIS sublattice.

B. Experimental details

Pure Nb metal sheet (0.004 inch in thickness, 3N5, from ESPI Metals) was used to prepare transmission electron microscopy (TEM) lamellae following conventional methods. We punched Ø3 mm discs from the metal sheet. They were mechanically polished to 50 μm, then dimpled to 10 μm, and finally ion milled (Gatan PIPS 691). The regions examined by HRTEM were ∼30 nm thick, as estimated by electron energy loss spectroscopy (EELS), while the areas selected for selected-area electron diffraction (SAED) also included regions thicker than 50 nm. To introduce oxygen into the thinned samples, one set of clean TEM lamellae (after ion milling) was exposed in air (humidity, 55%) for 48 h, and the others were treated by a plasma cleaner (Ar:O_2,

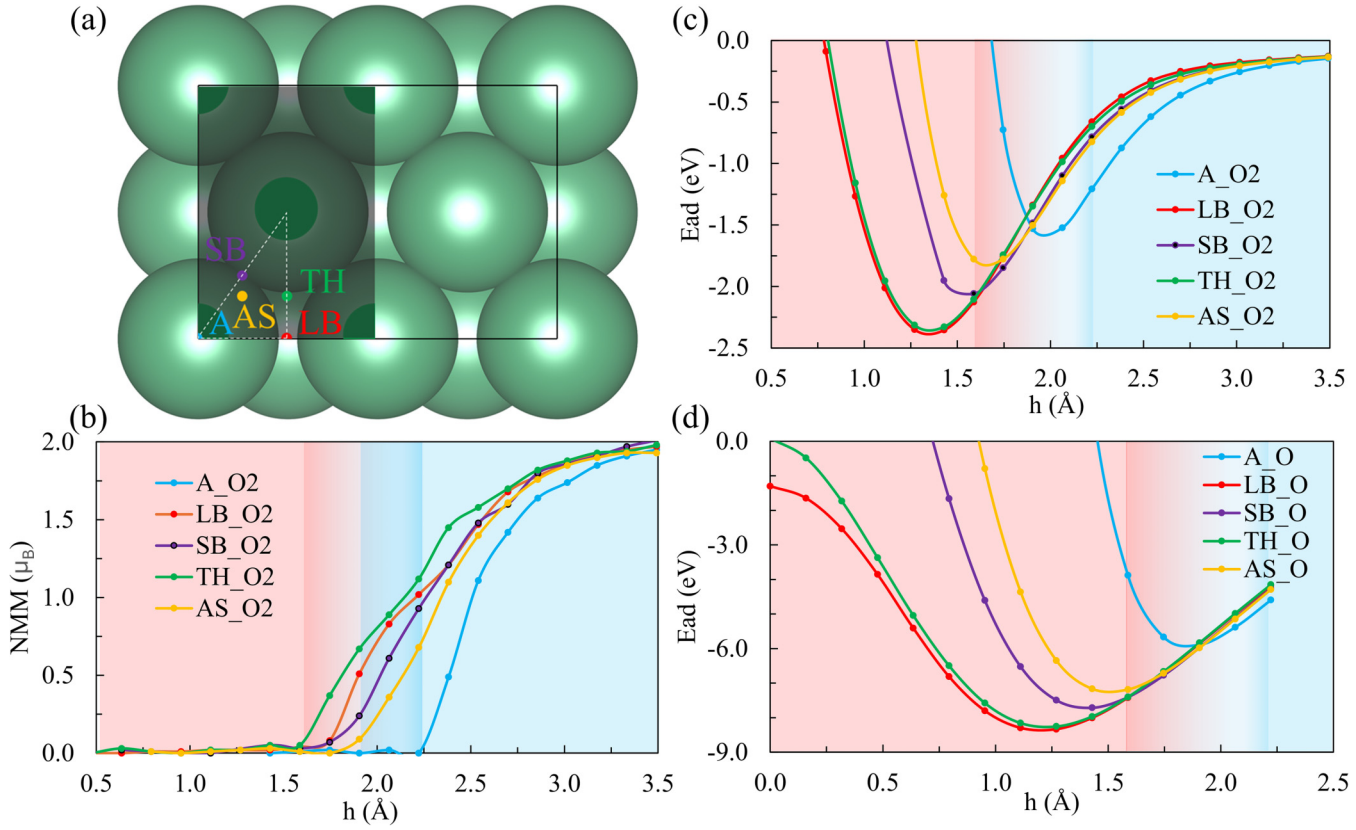


FIG. 1. Oxygen adsorption, dissociation, and penetration on the Nb(110) surface. (a) Surface structure and adsorption sites, including A, LB, SB, TH, and AS. (b) NMM during O_2 approach. (c), (d) Adsorption energies of molecular O_2 and atomic O as a function of distance from the surface. The shaded windows in panels (b)–(d) indicate three distinct regimes: a molecular adsorption window ($h \gtrsim 2.2$ Å, blue), a transition window (1.6 Å $\lesssim h \lesssim$ 2.2 Å, blue-to-red gradient), and an atomic penetration window ($h \lesssim 1.6$ Å, red).

80%:20%) for approximately 20 min. In both cases, TEM revealed the ordered ε phase described below rather than equilibrium niobium oxides. We performed SAED, TEM, HRTEM, and EELS on a Titan Cubed Themis 300 double Cs-corrected scanning/transmission electron microscope with a spatial resolution of 80 pm, operated at 200 kV. HRTEM image simulations were performed in the NCEMSS software package based on the multislice formulation of Cowley and Moodie [42].

III. RESULTS AND DISCUSSION

A. Oxygen adsorption and penetration on Nb(110)

To establish the initial stage of oxidation, we examine the interaction of O_2 with Nb surfaces using DFT calculations, focusing on the Nb(110) surface and comparing it with our previous study on Nb(100). We consider several representative adsorption sites on Nb(110), including atop (A), long bridge (LB), short bridge (SB), pseudo-three-fold hollow (TH), and an additional site (AS), as shown in Fig. 1(a).

We analyze O_2 dissociation based on the system's NMM [Fig. 1(b)]. As O_2 approaches the surface, the NMM decreases from its triplet ground state ($2\mu_B$) to zero, indicating progressive activation of O_2 and quenching of its gas-phase spin character by the Nb surface. Three regimes can be identified [Figs. 1(b)–1(d)]: molecular adsorption at large distances ($h \gtrsim 2.2$ Å, blue window), a transition region with progressive O_2 activation (1.6 Å $\lesssim h \lesssim$ 2.2 Å, gradient window), and an atomic-adsorption-dominated region at short distances ($h \lesssim$ 1.6 Å, red window).

At shorter distances, the strong quenching of the O_2 spin state indicates substantial activation by the Nb surface. The adsorption behavior in this region is therefore better described by the atomic-O adsorption energy shown in Fig. 1(d). Compared to molecular O_2, atomic O binds significantly more strongly to Nb. A clear site selectivity emerges: the LB site becomes strongly favored. Notably, at small distances, the LB site develops an additional driving force that pulls O atoms into the subsurface, which can be attributed to the larger geometric opening associated with this configuration. A similar behavior is observed on Nb(100) [30], where O_2 also approaches the surface via the A site at large distances, but penetrates through the hollow (H) site. The H site on Nb(100) corresponds to the most open surface geometry, analogous to the LB site on Nb(110). These results indicate that, although the specific entry sites depend on the surface orientation, O consistently penetrates into Nb through locations with relatively large openings.

Overall, oxygen penetration into Nb follows a geometry-driven mechanism. O_2 molecules approach the surface via atop sites, undergo surface-induced activation/dissociation, and the resulting atomic O preferentially penetrates through surface locations with larger geometric openings, such as the LB site on Nb(110) and the H site on Nb(100). This

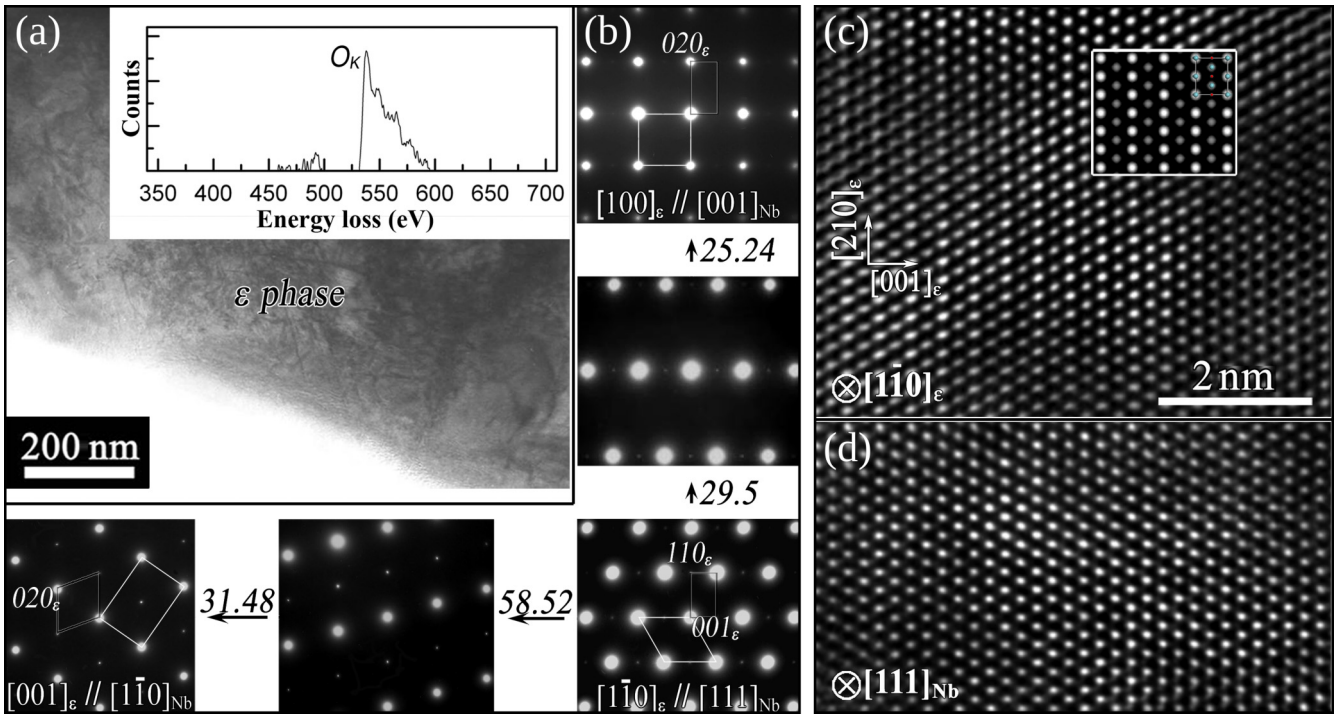


FIG. 2. TEM characterization of the ordered ε phase in partially oxidized Nb. (a) A typical TEM image of the ε phase. The inset in panel (a) shows an O_K edge in the EELS pattern. (b) Five SAED patterns of the ε phase. The rotation angles of the adjacent patterns are also given. (c) Experimental HRTEM image of the ε phase viewed along the $[1\bar{1}0]_\varepsilon$ direction. The small white box highlights a representative supercell showing the periodic contrast. The inset in panel (c) shows the corresponding simulated image generated using the NCEMSS software package based on the alternating layered configuration of O occupation in the ε phase, with the projected atomic positions of the ε unit cell overlaid. (d) Experimental HRTEM image of an untreated Nb lamella, prepared by the same procedure, viewed along $[111]_{Nb}$. Panels (a)–(c) were obtained from a lamella oxidized in air for 48 h.

establishes a direct link between surface dissociation and site-selective penetration, where wider openings facilitate O entry into the subsurface. This atomic-scale description of O penetration complements the Cabrera-Mott mechanism proposed for the growth of the native Nb oxide layer at room temperature [43].

B. TEM characterization of the ordered ε phase

Figure 2(a) shows the bright-field image of the partially oxidized region in the TEM sample. The inset displays an O_K edge in the EELS pattern, confirming the presence of O atoms. Diffraction analysis and HRTEM image simulation together reveal that oxygen incorporation into Nb forms a metastable Nb–O phase, which we denote as the ε phase. We determined the crystal structure of the ε phase from the SAED patterns in Fig. 2(b), with the corresponding rotation angles indicated. The primary diffraction spots are consistent with the bcc-Nb lattice (A2 type, space group: $Im\bar{3}m$), as marked by the white quadrangles. The weaker spots indicate a periodic modulation of the Nb lattice associated with the formation of a new ordered structure (ε phase). The ε phase is orthorhombic, with the space group *Cmmm* and lattice parameters $a_\varepsilon = 0.3301$ nm and $b_\varepsilon = c_\varepsilon = 0.4668$ nm, and the O atoms occupy OIS in an unsaturated state (see Appendix A for details).

We performed HRTEM measurements and image simulations. The experimental observations reveal the emergence of an ordered oxygen-containing phase during the early stage of oxidation. Figure 2(c) shows a representative HRTEM image of the oxidized Nb along the $[1\bar{1}0]_\varepsilon$ direction. In comparison with pristine Nb imaged along the corresponding direction in Fig. 2(d), the oxidized regions exhibit additional periodic weak contrast superimposed on the underlying bcc lattice. These features indicate ordered occupation of interstitial sites.

To determine the atomic configuration responsible for the observed contrast, we performed HRTEM image simulations using structural models with different oxygen occupancies. We find that a model in which O atoms occupy OIS in an alternating layered configuration (see Fig. 5 and Table II) reproduces the experimental images. As shown in the inset of Fig. 2(c), the simulated image accurately captures both the periodicity and weak contrast features observed experimentally. The resulting structure consists of alternating Nb and Nb + O planes, indicating that O atoms occupy OIS in alternating Nb planes. This ordered arrangement naturally explains the additional periodic contrast observed in the HRTEM images. Based on this experimentally validated structural motif, we identify the oxidized phase as an ordered ε phase formed during early oxidation. Because both the superlattice reflections in Fig. 2(b) and the additional periodic contrast in Fig. 2(c) are commensurate with the bcc-Nb lattice, the ε phase resides within the metallic Nb rather than within the native surface oxide, consistent with the enrichment of subsurface interstitial oxygen reported for Nb(110) [44]. The ε phase is an ordered interstitial phase formed at room temperature, distinct from the equilibrium niobium oxides NbO, NbO_2, and Nb_2O_5 [45].

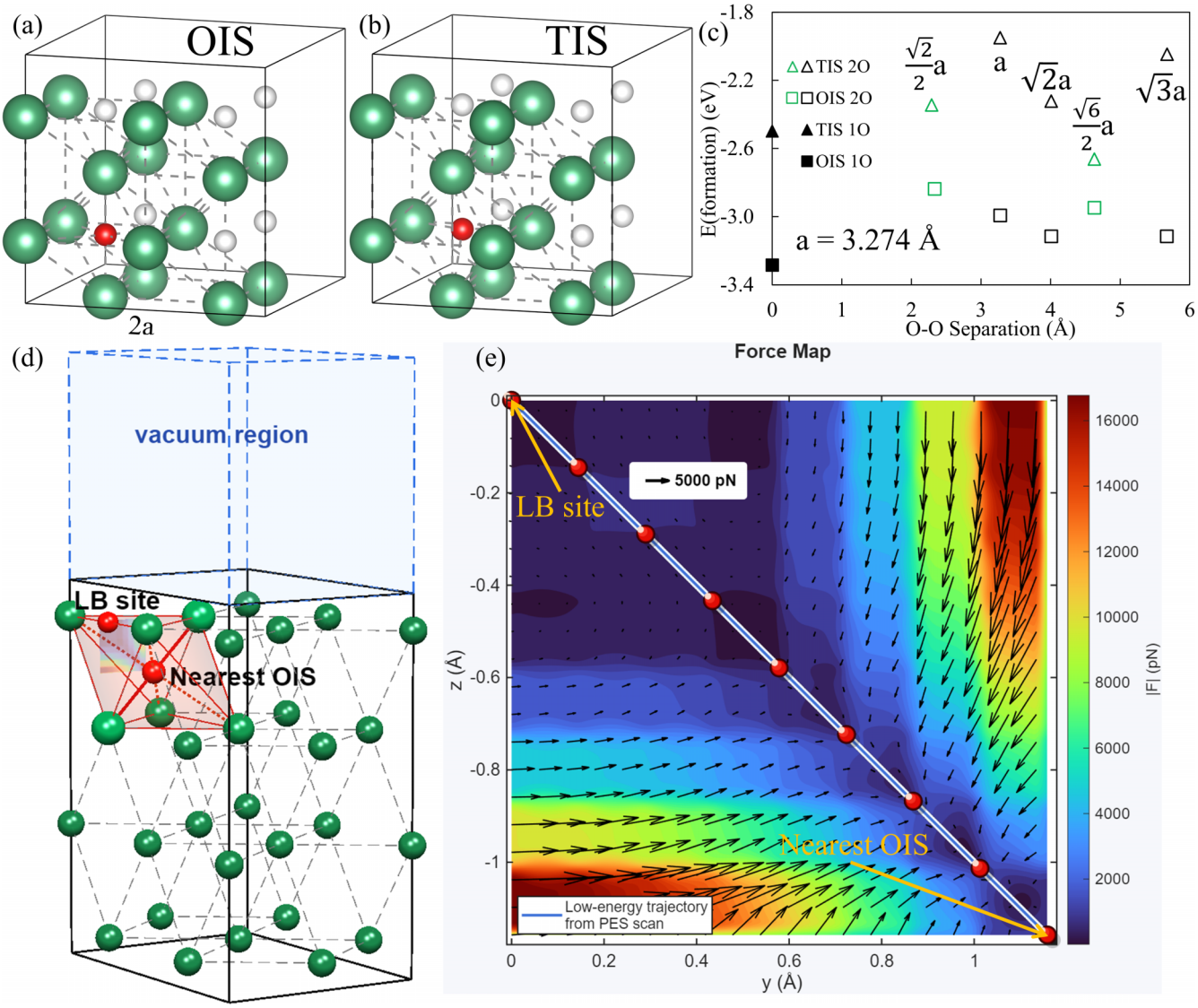


FIG. 3. Site preference and penetration pathway of interstitial oxygen in Nb. (a) Atomic model of the ε phase, in which O atoms occupy OIS in an alternating layered arrangement. Green: Nb; red: O; white: other available interstitial positions. (b) The corresponding TIS configuration. (c) Formation energy per O as a function of O–O separation. Filled symbols correspond to the one-O configurations, and open symbols correspond to two-O configurations. For the two-O cases, only OIS and TIS configurations with the same initial O–O separation are compared. Black symbols correspond to configurations consistent with the ε-phase arrangement, while green symbols represent configurations with O occupying other available positions. (d) Atomic model illustrating the geometrically open LB site and its connection to the nearest subsurface OIS. The force map in the yz plane along the LB-OIS pathway is embedded to show the local force field driving O penetration. (e) Force map in the yz plane showing the force acting on O during penetration from the LB site toward the nearest OIS, with the low-energy pathway obtained from the PES scan.

Identifying this ordered ε phase raises two related questions: How oxygen enters the Nb lattice and accesses favorable interstitial sites, and why the resulting oxygen-containing structure adopts an alternating layered arrangement. We address these questions below using DFT calculations of penetration pathways, interstitial-site preference, and concentration-dependent stability.

C. Interstitial site preference and penetration pathway

The HRTEM results indicate that the ε phase is characterized by O occupying OIS in an alternating layered configuration. To understand the origin of this structure, we compare the stability of O at OIS and TIS using DFT calculations. Figure 3(a) shows the ε-phase configuration with O at OIS. We construct the corresponding TIS configuration by translating the O atom along the x direction by $a/4$, as shown in Fig. 3(b). For a single O atom, the OIS configuration is significantly lower in energy (0.79 eV) than the TIS configuration, indicating that OIS is the preferred site. We then examine configurations containing two O atoms. Only OIS and TIS cases with the same initial O–O separation are compared. As shown in Fig. 3(c), OIS remains lower in energy than TIS for all separations. This trend holds for both configurations consistent with the ε-phase arrangement (black symbols)

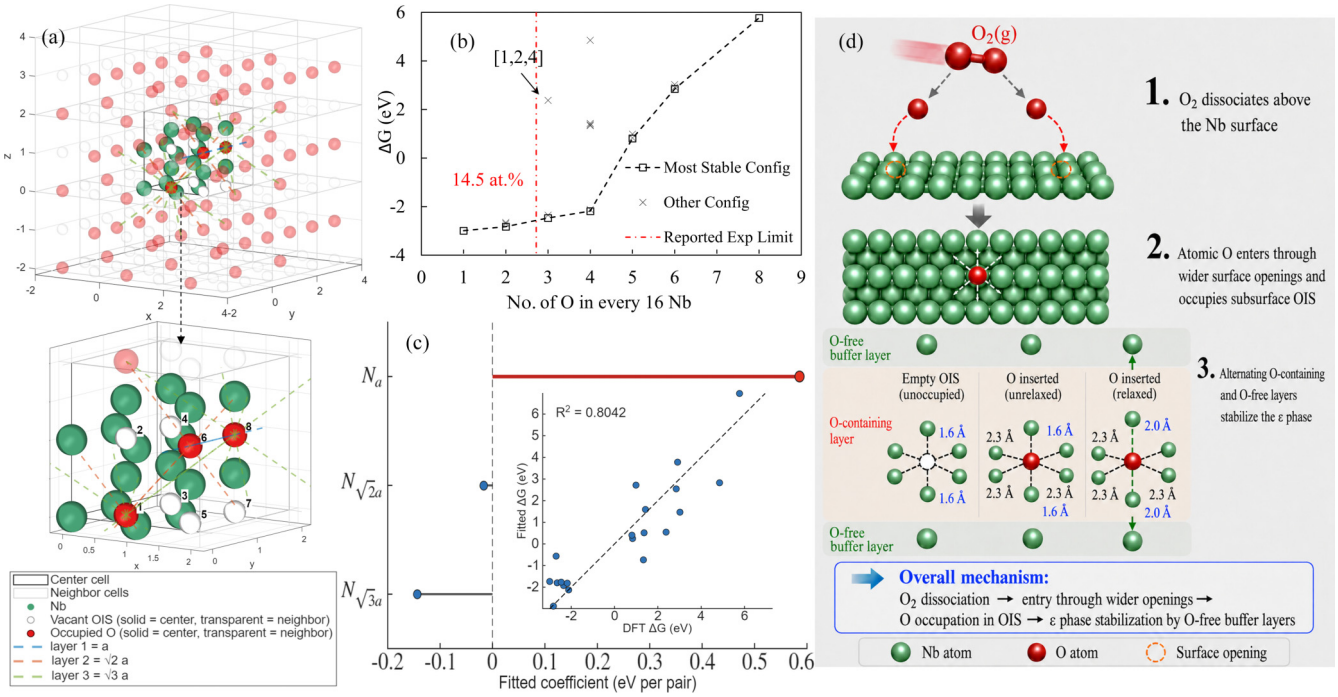


FIG. 4. Geometric origin of oxygen ordering and solubility limit in niobium. (a) Representative oxygen configurations based on the ε-phase lattice, illustrating the available interstitial sites and characteristic O–O separations (a, $\sqrt{2}a$, and $\sqrt{3}a$). An enlarged view of the central cell (indicated by a dashed arrow) labels the eight available oxygen sites (1–8) associated with the ordered ε-phase structure. (b) Change in Gibbs free energy ΔG as a function of oxygen concentration (number of O atoms per 16 Nb atoms). The most stable configurations at each concentration are connected by a dashed line, while other configurations are shown as crosses. The vertical dashed line indicates the experimental limit of $NbO_{0.17}$ (14.5 at. % O) reported for electrolytically prepared Nb(O) solid solutions [24], corresponding to ~2.7 O per 16 Nb. (c) Regression using geometric descriptors based on O–O separations. Fitted coefficients are shown together with the correlation between DFT-calculated and model-predicted ΔG (inset, $R^2 = 0.8042$). (d) Schematic illustration of the overall mechanism. All ΔG values in panels (b)–(c) are reported per O atom.

and those where O occupies other available positions (green symbols).

Having established the thermodynamic preference for OIS occupation, we further examine how oxygen can access these sites during penetration from the surface. Figure 3(d) illustrates the geometric connection between the open LB site on Nb(110) and the nearest subsurface OIS. To quantify this connection, we performed a two-dimensional PES scan in the yz plane along the LB-OIS pathway. The resulting force map in Fig. 3(e) shows that, once O enters through the LB site, the local force field directs it toward the nearest OIS. The low-energy trajectory obtained from the PES scan therefore provides a mechanistic link between the geometry-selected surface entry site and the preferred subsurface interstitial configuration.

Analysis of the relaxed structures shows that this preference is governed by the local Nb–O bonding geometry. In both OIS and TIS, Nb–O bond lengths are similar (~2.0 Å), while the coordination differs: O in OIS bonds with two Nb atoms, whereas in TIS it is coordinated by four. This preference suggests that the relaxed OIS geometry provides a more favorable local Nb–O coordination environment, with near-optimal Nb–O distances achieved without imposing excessive constraints on the surrounding Nb lattice. These results highlight the dominant role of local Nb–O environments in determining stability. This local bonding preference also clarifies why the ε phase adopts an alternating layered arrangement rather than a uniformly oxygen-filled interstitial lattice. Oxygen incorporation produces local distortions around occupied OIS. When O atoms occupy every adjacent layer, these distortions overlap and impose a larger elastic penalty on the Nb framework. In contrast, the alternating layered ε structure separates O-containing layers by O-free Nb layers. These O-free layers provide structural flexibility and serve as buffer layers, allowing the lattice to accommodate local Nb–O distortions while preserving the overall Nb framework.

D. Oxygen ordering and the concentration limit

Building on the connection between surface penetration and OIS occupation, we next examine how multiple incorporated O atoms arrange within the OIS sublattice. Using this sublattice as the structural framework for subsequent oxygen incorporation and ordering, we evaluate the relative stability of different multi-O configurations in a Nb supercell derived from the experimentally identified ε phase. As shown in Fig. 4(a), this supercell contains eight available oxygen sites, labeled from 1 to 8. A representative configuration with three oxygen atoms occupying sites [1,6,8] is illustrated, together with the corresponding O–O separations at characteristic distances.

Figure 4(b) compares ΔG for the three possible three-O configurations: [1, 6, 8], [1, 2, 4], and [1, 4, 6]. Among these, [1, 2, 4] is significantly less favorable, whereas the other two

exhibit comparable stability. Since these configurations differ primarily in their O–O separations, this comparison suggests that geometric factors associated with O–O distances play an important role in determining stability.

To further quantify this effect, we construct a simple linear model based on the counts of O–O pairs at characteristic separation distances (N_a, $N_{\sqrt{2}a}$, and $N_{\sqrt{3}a}$). Figure 4(c) shows the fitted coefficients. The coefficient for N_a is positive and substantially larger than those for the longer-distance pair counts, indicating that O–O pairs at a separation of a impose the strongest energetic penalty. The correlation between predicted and DFT-calculated ΔG [Fig. 4(c), inset] shows that this simple geometric model captures the dominant trend in ΔG.

These results indicate that O–O separations serve as effective geometric descriptors for capturing the stability of oxygen configurations, particularly through the energetic penalty associated with O–O arrangements. As the oxygen concentration increases, configurations inevitably introduce O–O pairs at short separation distances. This leads to a rapid increase in ΔG and provides a geometric origin for the experimentally reported concentration limit in electrolytically prepared Nb(O) solid solutions [24].

We further examined the effect of supercell size (Fig. 6). Scaling down to a $1 \times 1 \times 1$ cell gives a ΔG essentially identical to that of the corresponding $2 \times 2 \times 2$ configuration. Representative calculations using a larger $4 \times 4 \times 4$ supercell reproduce the energetic trend of the $2 \times 2 \times 2$ calculations at low and intermediate O concentrations, where the ε framework remains relatively stable. At high O concentration, however, the larger cell permits more extensive structural relaxation, and the ε framework undergoes pronounced structural collapse. Thus, the rapid increase in ΔG in the smaller cell and the structural collapse in the larger cell both indicate a loss of stability of the ε structure at high O concentration.

IV. CONCLUSIONS

In this work, we present a unified picture of early-stage oxidation in Nb by combining first-principles calculations with HRTEM observations. We identify an ordered ε phase in which O atoms occupy OIS in an alternating layered configuration, consistent with experimental imaging.

By analyzing O_2 dissociation and penetration pathways, we show that oxygen incorporation into Nb is governed by surface geometry, where O_2 dissociates above the surface and atomic O preferentially enters through sites with larger geometric openings. This connects surface processes to OIS occupation and provides an atomistic entry point for understanding subsequent ε-phase ordering.

At the bulk level, O energetically favors OIS over TIS due to its local bonding environment. The alternating layered ε phase further stabilizes incorporated oxygen by separating O-containing layers with O-free Nb layers, which buffer local O-induced distortions and reduce the elastic penalty associated with oxygen incorporation. As oxygen concentration increases, short-range O–O interactions become increasingly unavoidable, driving a rapid increase in ΔG. Thus, oxygen incorporation, ordering, and thermodynamic stability in Nb can be understood within a geometry-driven framework: Surface geometry guides oxygen entry, local Nb–O bonding favors OIS occupation, alternating O-containing/O-free layers stabilize the ε phase, and short O–O separations limit further oxygen incorporation.

More broadly, these results demonstrate that oxygen ordering and solubility limit in Nb can be understood in terms of simple geometric constraints. This perspective provides a physically transparent framework for understanding oxygen behavior in Nb and potentially other bcc metal-oxygen systems. It may also serve as a starting point for developing more comprehensive descriptions of oxygen behavior in Nb, where complex structural evolution and diverse electronic properties are known to emerge across a wide range of compositions [3].

ACKNOWLEDGMENTS

We acknowledge the support from the Innovation Award of J. Insley Blair-Pyne Fund, the Evin-Catalysis Initiative Award, and the Fund from the Dean for Research at Princeton. The Texas Advanced Computing Center (TACC) provided computational resources. This research used the Imaging and Analysis Center at Princeton University, partly supported by the Princeton Center for Complex Materials, a National Science Foundation Materials Research Science and Engineering Center (Grant No. DMR-2614599). G.C. thanks Dr. Lianlong He for valuable assistance with the experimental part of this work.

The authors have no conflicts to disclose.

DATA AVAILABILITY

The data that support the findings of this study are available from the corresponding author upon reasonable request.

APPENDIX A: STRUCTURE DETERMINATION OF THE ε PHASE

The five SAED patterns in Fig. 2(b), together with the rotation angles between the adjacent patterns, show unequivocally that the ε phase possesses an orthorhombic crystal structure with the point group *mmm*. The bright spots correspond completely to the period of bcc-Nb, while the weak spots show a periodic change of the bcc-Nb lattice, the corresponding plane spacings being changed accordingly. Taking the lattice parameter of the Nb phase as $a_{\mathrm{Nb}} = 0.3301$ nm, the lattice parameters of the ε phase are calculated from the relationship between the ε and Nb reflections in the composite patterns by an internal standard method: $a_\varepsilon = 0.3301$ nm, $b_\varepsilon = 0.4668$ nm, and $c_\varepsilon = 0.4668$ nm. Based on the reflections observed

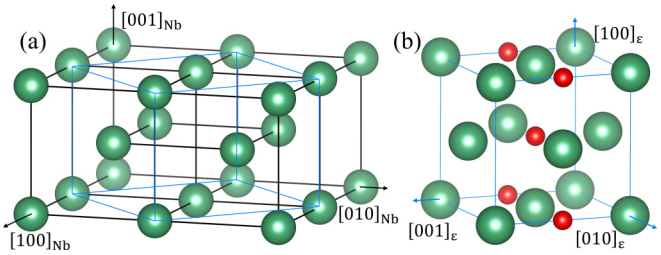


FIG. 5. (a) A lattice model to illustrate the phase transformation from bcc-Nb to the ε phase. (b) The proposed crystal structure of the ε phase with oxygen at (0, 0, 1/2).

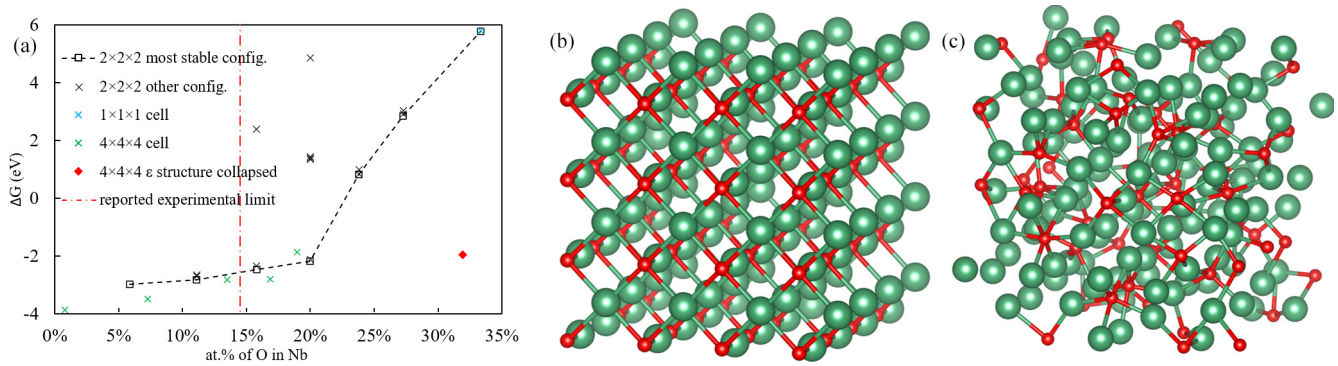


FIG. 6. (a) Change in ΔG as a function of O concentration for $1 \times 1 \times 1$, $2 \times 2 \times 2$, and $4 \times 4 \times 4$ Nb supercells. The $4 \times 4 \times 4$ calculations reproduce the energetic trend obtained with the $2 \times 2 \times 2$ cell at low and intermediate O concentrations. At 31.91 at. % O ($Nb_{128}O_{60}$), however, the ε structure in the $4 \times 4 \times 4$ cell undergoes structural collapse during relaxation and is therefore shown separately. The vertical red dashed line indicates the reported experimental limit. (b), (c) Initial and relaxed structures, respectively, of the $4 \times 4 \times 4$ cell containing 60 O atoms, illustrating the pronounced structural collapse at high O concentration. All ΔG values are reported per O atom. Green: Nb; red: O.

to be absent, the Bravais lattice of the ε phase is base-centered orthorhombic and the space group is *Cmmm*.

The ε phase can therefore be described as a Nb supercell, marked by the dashed lines in Fig. 5(a). Filling this supercell according to the character of the space group *Cmmm* places Nb on the 2*a* and 2*c* positions and leaves four equivalent positions that coincide with OIS or TIS of the Nb supercell as the possible sites for O (Table II). The structure obtained with O on 2*d* (0, 0, 1/2) is shown in Fig. 5(b). If this site were fully occupied, one cell would contain four Nb and two O atoms, corresponding to a limiting composition of Nb_2O (33.3 at. % O).

The three remaining candidates: 8*n* (0, 1/4, 1/4) (OIS), 8*m* (1/4, 1/4, 1/4) (TIS), and 8*n* (0, 3/8, 1/8) (TIS) were also examined. All of them have a much higher oxygen content in a unit cell (NbO_2 rather than Nb_2O), and the distances between the two nearest oxygen atoms, or between Nb and oxygen atoms, are so short that the atoms cannot be occupied at the same time. Moreover, their reflection conditions do not agree with our experimental results.

The lattice parameters of the Nb supercell are, however, not measurably changed by the diffusion of oxygen atoms, which indicates that the 2*d* sites are far from fully occupied and that the oxygen content of the ε phase is well below 33.3 at. %. Its precise value cannot be determined from the present measurements. The oxygen atoms in the ε structure are therefore in an unsaturated state and occupy the 2*d* equivalent positions randomly (Table II). This is consistent with our first-principles calculations, which show that at 31.91 at. % O, close to the composition of a fully occupied Nb_2O, the ε framework collapses during structural relaxation (Fig. 6). The proposed atomic model is further verified by HRTEM imaging and the corresponding image simulation.

APPENDIX B: LINEAR REGRESSION MODEL FOR OXYGEN-OXYGEN INTERACTION

Throughout this analysis, ΔG is reported per O atom. To quantify the effect of oxygen distribution on thermodynamic stability, we construct a linear model based on O–O pair counts at characteristic separations. The Gibbs free energy is expressed as

$$\Delta G = \alpha + c_1 N_a + c_2 N_{\sqrt{2}a} + c_3 N_{\sqrt{3}a},$$

where N_a, $N_{\sqrt{2}a}$, and $N_{\sqrt{3}a}$ denote the numbers of O–O pairs separated by distances a, $\sqrt{2}a$, and $\sqrt{3}a$, respectively, within the octahedral interstitial sublattice. The fitted coefficients are $\alpha = -1.7314$ eV, $c_1 = 0.5856$ eV per pair, $c_2 = -0.0164$ eV per pair, and $c_3 = -0.1432$ eV per pair. The coefficient of determination is $R^2 = 0.8042$, indicating that the model captures the dominant correlation between O–O arrangements and ΔG.

Pair counts are evaluated for periodically repeated configurations. For each configuration, O atoms in the central cell are paired with those in neighboring periodic images, and the total counts are divided by 2 to obtain unique pair multiplicities per cell.

Table I lists all configurations used in the regression, along with the corresponding pair counts, DFT-calculated ΔG, and model-predicted ΔG.

APPENDIX C: SUPERCELL-SIZE DEPENDENCE AND STRUCTURAL RELAXATION

To examine the effect of supercell size, we performed additional calculations using both smaller and larger Nb supercells, as summarized in Fig. 6. All ΔG values discussed below are reported per O atom.

We first scaled the $2 \times 2 \times 2$ supercell used in the main calculations down to a $1 \times 1 \times 1$ cell. Because the $1 \times 1 \times 1$ bcc cell contains only two Nb atoms, introducing a single O atom already corresponds to an O concentration of 33.3 at. %. Therefore, only one configuration can be directly compared with the $2 \times 2 \times 2$ calculations. As shown in Fig. 6(a), the ΔG obtained with the $1 \times 1 \times 1$ cell is essentially identical to that of the corresponding $2 \times 2 \times 2$ configuration. This agreement confirms the consistency of the calculated energy for the same periodically repeated structure upon scaling down the supercell.

We then increased the supercell size to $4 \times 4 \times 4$. Compared with the $2 \times 2 \times 2$ cell, the larger supercell contains

substantially more structural and configurational degrees of freedom, making an exhaustive calculation of all possible O configurations computationally impractical. We therefore examined representative configurations at several O concentrations. At low and intermediate O concentrations, where the ε structure is maintained after relaxation, the $4 \times 4 \times 4$ calculations reproduce the energetic trend obtained with the $2 \times 2 \times 2$ cell [Fig. 6(a)]. This indicates that the $2 \times 2 \times 2$ cell provides a reasonable description of the energetics in this concentration range.

At high O concentration, however, the larger supercell shows qualitatively different structural behavior. In the $2 \times 2 \times 2$ cell, the stronger periodic constraint limits long-range structural relaxation, and the destabilization at high O loading is mainly reflected by the rapid increase in ΔG. In contrast, the $4 \times 4 \times 4$ cell allows more extensive long-range and symmetry-breaking relaxation. For the $Nb_{128}O_{60}$ configuration, corresponding to 31.91 at. % O, the initially constructed ε structure undergoes pronounced structural collapse during relaxation [Figs. 6(b) and 6(c)]. Eighty-two percent of the O atoms are displaced by more than 0.5 Å and 48% are displaced by more than 1.0 Å. These large collective displacements indicate that the relaxed structure can no longer be described as the original ε structure.

The scaling calculations therefore show two different manifestations of the effect of high O loading. In the smaller cell, the ε structure is strongly constrained by periodicity, and its destabilization is reflected by a rapid increase in ΔG. In the larger cell, additional relaxation degrees of freedom allow the system to lower its energy by leaving the ε structural framework, resulting in structural collapse. At lower O concentrations, before this collapse occurs, the $4 \times 4 \times 4$ calculations remain consistent with the energetic trend obtained using the $2 \times 2 \times 2$ cell.

APPENDIX D: ADDITIONAL TABLES

This Appendix collects the tabulated data used in the preceding analysis. Table I lists the oxygen configurations considered in the linear regression of Appendix B, together with the corresponding O–O pair counts and the DFT-calculated and fitted Gibbs free energies per O atom. Table II lists the Wyckoff positions of *Cmmm* that coincide with octahedral or tetrahedral interstitial sites of the Nb supercell, as used in the structure determination of Appendix A.

TABLE I. Oxygen configurations and corresponding geometric parameters, together with DFT and fitted Gibbs free energies per O.

Occ sites	N_a	$N_{\sqrt{2}a}$	$N_{\sqrt{3}a}$	ΔG (DFT, eV)	ΔG (fit, eV)
1	0	0	0	−2.9919	−1.7314
1, 8	0	0	8	−2.8237	−2.8768
1, 7	0	4	0	−2.6559	−1.7969
1, 5	2	0	0	−2.7010	−0.5602
1, 4, 6	0	12	0	−2.3486	−1.9278
1, 6, 8	2	4	8	−2.4661	−1.7710
1, 2, 4	4	4	0	2.3746	0.5455
1, 4, 6, 7	0	24	0	−2.1224	−2.1242
1, 3, 6, 8	4	8	16	−2.1832	−1.8106
1, 6, 7, 8	4	12	8	1.3340	−0.7307
1, 2, 6, 8	6	8	8	1.3721	0.5059
1, 2, 3, 5	6	12	0	1.4291	1.5858
1, 2, 3, 4	8	8	0	4.8493	2.8225
1, 2, 3, 5, 8	6	24	8	0.8312	0.2441
1, 3, 4, 6, 8	8	16	16	0.8073	0.4009
1, 2, 4, 6, 8	10	16	8	0.9880	2.7174
1, 3, 4, 5, 6, 8	12	24	24	3.0243	1.4671
1, 3, 4, 6, 7, 8	12	28	16	2.8427	2.5469
1, 3, 4, 5, 7, 8	14	24	16	2.9161	3.7836
1, 2, 3, 4, 5, 6, 7, 8	24	48	32	5.7707	6.9562

TABLE II. Equivalent positions for the ε phase with the space group of *Cmmm*. The four O positions listed are the Wyckoff positions of *Cmmm* that coincide with OIS or TIS of the Nb supercell; only the 2*d* position is consistent with the experimental diffraction patterns.

No.	Equivalent positions			Atom
1	2*a*	*mmm*	0, 0, 0	Nb
2	2*c*	*mmm*	1/2, 0, 1/2	Nb
3	2*d*	*mmm*	0, 0, 1/2	O (OIS)
4	8*n*	*m*	0, 1/4, 1/4	O (OIS)
5	8*m*	2	1/4, 1/4, 1/4	O (TIS)
6	8*n*	*m*	0, 3/8, 1/8	O (TIS)

[1] P. Kofstad, *High Temperature Corrosion* (Elsevier Applied Science, London, 1988).

[2] D. J. Young, *High Temperature Oxidation and Corrosion of Metals*, 2nd ed. (Elsevier, Amsterdam, 2016), Vol. 1.

[3] R. J. Cava, B. Batlogg, J. J. Krajewski, H. F. Poulsen, P. Gammel, W. F. Peck, and L. W. Rupp, Electrical and magnetic properties of $Nb_2O_{5-\delta}$ crystallographic shear structures, Phys. Rev. B **44**, 6973 (1991).

[4] C. Liu, L. Yu, Y. Liu, Z. Ma, H. Li, C. Li, and C. Liu, Interactions between interstitial oxygen and substitutional niobium atoms in Ti–Nb–O BCC alloys: First-principles calculations, AIP Adv. **10**, 025309 (2020).

[5] L. Wu, A. Wang, J. Cui, Z. Li, J. Zhang, Y. Ma, J. Wang, P. Zhao, T. Yu, G. Liang, Z. Qian, and G. Zhang, First-principles study of the diffusion behavior of gaseous elements (H, N, O) in niobium and their effects on electron transport properties, J. Alloys Compd. **1055**, 186488 (2026).

[6] G. Fulton and A. Lunev, Probing the correlation between phase evolution and growth kinetics in the oxide layers of tungsten using Raman spectroscopy and EBSD, Corros. Sci. **162**, 108221 (2020).

[7] P. Kofstad and O. J. Krudtaa, High temperature metallographic microscope studies of the initial oxidation of tantalum, J. Less-Common Met. **5**, 477 (1963).

[8] K. G. Gareev, Diversity of iron oxides: Mechanisms of formation, physical properties and applications, Magnetochemistry **9**, 119 (2023).

[9] Y. Xing, I. Kim, K. T. Kang, B. Park, Z. Wang, J. Chan Kim, H. Y. Jeong, W. S. Choi, J. Lee, and S. H. Oh, Atomic-scale operando observation of oxygen diffusion during topotactic phase transition of a perovskite oxide, Matter **5**, 3009 (2022).

[10] J. van Landuyt, R. Gevers, and S. Amelinckx, Ordering of interstitial impurities in niobium, Phys. Status Solidi B **13**, 467 (1966).

[11] D. Gunwaldsen and D. Potter, A long period superlattice in dilute vanadium-oxygen alloys, J. Less-Common Met. **34**, 97 (1974).

[12] F. F. Milillo and D. I. Potter, Interstitial ordering and precipitation in dilute Ta-O alloys at 100 to 270°C, Metall. Trans. A **9**, 283 (1978).

[13] T. Moriya and H. Ino, Ordered structures of interstitial solutes in BCC lattice, J. Phys. Soc. Jpn. **46**, 1776 (1979).

[14] A. Anferov, S. P. Harvey, F. Wan, J. Simon, and D. I. Schuster, Superconducting qubits above 20 GHz operating over 200 mK, PRX Quantum **5**, 030347 (2024).

[15] P. Tsakiropoulos, On Nb silicide based alloys: Alloy design and selection, Materials **11**, 844 (2018).

[16] K. Babaei, A. Fattah-alhosseini, and R. Chaharmahali, A review on plasma electrolytic oxidation (PEO) of niobium: Mechanism, properties and applications, Surf. Interfaces **21**, 100719 (2020).

[17] C. Reynolds, T. M. Pollock, and A. Van der Ven, Solute-solute interactions in dilute Nb-X-O alloys from first principles, Acta Mater. **266**, 119621 (2024).

[18] G. Ciovati, Improved oxygen diffusion model to explain the effect of low-temperature baking on high field losses in niobium superconducting cavities, Appl. Phys. Lett. **89**, 022507 (2006).

[19] C. A. Marrache-Kikuchi, H. Aubin, A. Pourret, K. Behnia, J. Lesueur, L. Bergé, and L. Dumoulin, Thickness-tuned superconductor-insulator transitions under magnetic field in *a*-NbSi, Phys. Rev. B **78**, 144520 (2008).

[20] C. Nico, T. Monteiro, and M. P. F. Graça, Niobium oxides and niobates physical properties: Review and prospects, Prog. Mater Sci. **80**, 1 (2016).

[21] S. Berman, A. Zhussupbekova, B. Walls, K. Walshe, S. I. Bozhko, A. Ionov, D. D. O'Regan, I. V. Shvets, and K. Zhussupbekov, Unraveling the atomic and electronic structure of nanocrystals on superconducting Nb(110): Impact of the oxygen monolayer, Phys. Rev. B **107**, 165425 (2023).

[22] C. Reynolds, T. M. Pollock, and A. Van der Ven, Prediction of Nb–O phase stability and analysis of common defects in BCC Nb and vacancy-ordered rocksalt NbO, Metall. Mater. Trans. A **57**, 1490 (2026).

[23] R. D. Veit, N. A. Kautz, R. G. Farber, and S. J. Sibener, Oxygen dissolution and surface oxide reconstructions on Nb(100), Surf. Sci. **688**, 63 (2019).

[24] A. V. Arakcheeva, V. V. Grinevich, G. Chapuis, and V. F. Shamrai, Structure studies of solid solutions of oxygen in electrolytic niobium, Crystallogr. Rep. **47**, 237 (2002).

[25] A. R. Massih and R. J. Pérez, Thermodynamic evaluation of the Nb-O system, Technical Report No. PM 05-002 v2, Quantum Technologies AB, Uppsala, Sweden, 2006.

[26] P. Hu, P. Hu, T. D. Vu, M. Li, S. Wang, Y. Ke, X. Zeng, L. Mai, and Y. Long, Vanadium oxide: Phase diagrams, structures, synthesis, and applications, Chem. Rev. **123**, 4353 (2023).

[27] M. Wen, B. An, S. Fukuyama, and K. Yokogawa, First-principles study of oxidized Nb(100) surface structures, Surf. Sci. **603**, 216 (2009).

[28] B. An, S. Fukuyama, K. Yokogawa, and M. Yoshimura, Surface structures of clean and oxidized Nb(100) by LEED, AES, and STM, Phys. Rev. B **68**, 115423 (2003).

[29] I. Arfaoui, J. Cousty, and H. Safa, Tiling of a Nb(110) surface with NbO crystals nanosized by the NbO/Nb misfit, Phys. Rev. B **65**, 115413 (2002).

[30] D. Fan, G. Cheng, D. Nashine, and N. Yao, Dissociative chemisorption pathways of oxygen on Nb(100) surface: A first-principles study, J. Appl. Phys. **138**, 025302 (2025).

[31] D. N. Tafen and M. C. Gao, Oxygen atom adsorption on and diffusion into Nb(110) and Nb(100) from first principles, JOM **65**, 1473 (2013).

[32] Q.-G. Wang and J.-X. Shang, First-principles study on the incipient oxidization of Nb(110), J. Phys. Condens. Matter **24**, 225005 (2012).

[33] P. P. Matyash, N. A. Skakun, and N. P. Dikii, Use of proton channeling to determine the location of oxygen dissolved in a niobium single crystal, Pis'ma Zh. Eksp. Teor. Fiz. **19**, 31 (1974) [JETP Lett. **19**, 18 (1974)].

[34] R. E. Kaim and D. W. Palmer, Irradiation-induced lattice–site change of oxygen in niobium, Philos. Mag. A **40**, 279 (1979).

[35] J. R. Chelikowsky, N. Troullier, and Y. Saad, Finite-difference-pseudopotential method: Electronic structure calculations without a basis, Phys. Rev. Lett. **72**, 1240 (1994).

[36] J. R. Chelikowsky, The pseudopotential-density functional method applied to nanostructures, J. Phys. D Appl. Phys. **33**, R33 (2000).

[37] N. Troullier and J. L. Martins, Efficient pseudopotentials for plane-wave calculations, Phys. Rev. B **43**, 1993 (1991).

[38] J. P. Perdew and Y. Wang, Accurate and simple analytic representation of the electron-gas correlation energy, Phys. Rev. B **45**, 13244 (1992).

[39] H. J. Monkhorst and J. D. Pack, Special points for Brillouin-zone integrations, Phys. Rev. B **13**, 5188 (1976).

[40] P. Chen, D. Fan, A. Selloni, J. Fan, and N. Yao, Anomalous saturation of CO adsorption at 26% on Cu(111) Governed by nanometer-scale substrate-mediated interactions, J. Am. Chem. Soc. **148**, 360 (2026).

[41] M. Sakurai, R. Wang, T. Liao, C. Zhang, H. Sun, Y. Sun, H. Wang, X. Zhao, S. Wang, B. Balasubramanian, X. Xu, D. J. Sellmyer, V. Antropov, J. Zhang, C.-Z. Wang, K.-M. Ho, and J. R. Chelikowsky, Discovering rare-earth-free magnetic materials through the development of a database, Phys. Rev. Mater. **4**, 114408 (2020).

[42] J. M. Cowley and A. F. Moodie, The scattering of electrons by atoms and crystals. I. A new theoretical approach, Acta Crystallogr. **10**, 609 (1957).

[43] M. Grundner and J. Halbritter, On the natural Nb_2O_5 growth on Nb at room temperature, Surf. Sci. **136**, 144 (1984).

[44] M. Delheusy, A. Stierle, N. Kasper, R. P. Kurta, A. Vlad, H. Dosch, C. Antoine, A. Resta, E. Lundgren, and J. Andersen, X-ray investigation of subsurface interstitial oxygen at Nb/oxide interfaces, Appl. Phys. Lett. **92**, 101911 (2008).

[45] R. Elliott, Columbium-oxygen system, Trans. Am. Soc. Metals **52**, 990 (1960).